Article

Extended State Observer-Based Predictive Current Control for Dual Three-Phase PMSM with High Dynamic Performance

Huanli Liu [ID], **Dayu Luo** [ID] **and Weiyang Lin** *[ID]

Research Institute of Intelligent Control and Systems, Harbin Institute of Technology, Harbin 150001, China; hlliu@stu.hit.edu.cn (H.L.); 23s104088@stu.hit.edu.cn (D.L.)
* Correspondence: wylin@hit.edu.cn

Abstract: Model predictive controllers are widely discussed in the field of dual three-phase permanent magnet synchronous motor control. However, conventional predictive current controllers usually suffer from parameter inaccuracies or model uncertainties, resulting in prediction errors and deterioration of control performance. Therefore, in this paper, an extended state observer-based (ESO) model predictive current controller is proposed to effectively improve the dynamic performance of the motor and its robustness to parameters or disturbances. Parameter inaccuracies or model uncertainties are considered to be lumped disturbances and expressed in the modified mathematical model of the motor. Then, with the designed observer estimating the external disturbances in real time, the prediction error is compensated and corrected periodically. Additionally, the parameter design method of the observer is presented to simplify the controller design. Finally, comparative experiments are implemented to sufficiently demonstrate the effectiveness of the proposed method for dynamic performance improvement as well as for parameter robustness. The results show that the proposed method takes only 17 µs of computation time with a closed-loop bandwidth of 1839 rad s^{-1}. In addition, the maximum d-axis following error of the proposed method is only 0.10 A in the load dynamics experiments, which is a significant improvement compared to the 0.79 A of the traditional proportional-integral controller.

Keywords: extended state observer; model predictive current control; dual-three phase motor; parameter uncertainty

1. Introduction

The dual three-phase permanent magnet synchronous motor (DTP-PMSM) has received significant attention from researchers in recent years due to the fault-tolerant performance of its extra winding [1–4]. Additionally, the requirement for inverter capacity is halved since the additional set of winding shares the phase currents of the motor at the same torque. As a result, DTP-PMSMs are widely used in the fields of ship propulsion, electric vehicles, and other high-power applications [5–7].

Traditional control methods based on field-oriented control have been widely applied to three-phase motors, which effectively simplifies the motor control [8]. However, the method cannot be directly applied to DTP-PMSM due to the presence of greater degrees of freedom. Therefore, the vector space decoupling (VSD) based theoretical method is proposed to be applied to the torque control of multiphase motors [9]. The method transforms the six-phase current or voltage components into the electromechanical energy conversion subspace and the harmonic component subspace, respectively. The electromechanical energy subspace is used to control the output torque, while the harmonic component subspace is used to control the current harmonic components of the motor. Thereafter, four conventional proportional-integral (PI) controllers are utilized to control these two subspaces, which enable effective control of both the torque and harmonic components of the DTP-PMSM. Nevertheless, subject to the bandwidth performance of the PI controllers, it is challenging to further improve the dynamic performance for high-performance servo control applications.

Among several existing techniques, the model predictive current controller (MPCC) is a satisfactory and easy-to-implement high-performance solution [10–12]. At each control period, MPCC predicts the current using the mathematical model of the motor in order to calculate the optimal control result; thus, the dynamic performance of the current is significantly improved. The existing literature generally categorizes MPCC as finite control set MPCC (FCS-MPCC) and continuous control set MPCC (CCS-MPCC) [13]. The FCS-MPCC searches all available voltage vectors in the inverter and selects the optimal one to apply directly to the motor, therefore providing an adequately high bandwidth. In [14], the authors introduced the concept of virtual vectors to realize robust FCS-MPCC. Additionally, literature [15] presents a space vector-optimized predictive controller to deal with fast current response by presynthesizing space vectors, which improves the dynamic response performance. However, the existing FCS-MPCC needs to search a large number of available vectors, especially when dealing with multi-step prediction. Therefore, such methods usually require a great computational effort for DTP-PMSM [16].

As another class of MPCC methods, CCS-MPCC computes the optimal voltage vector in the whole vector plane directly, avoiding the searching process and thus providing better computational efficiency [17]. In [18], the authors implemented a generalized CCS-MPCC to efficiently increase the torque density. In [19], the scheme of open-switch fault is analyzed in detail, and a high control bandwidth CCS-MPCC under the fault-tolerant operation is proposed. Despite the promising results, conventional MPCC inevitably suffers from prediction errors caused by parameter uncertainties or model nonlinearities such as dead time, resulting in deteriorating performance [20]. To address this problem, researchers have studied a number of possible approaches [21–24]. In [21], a sliding mode observer (SMO) based MPCC is proposed to eliminate the effects of motor parameters and unmodeled dynamics. Further, one study [22] couples an SMO with a generalized proportional-integral observer for fast-tracking of time-varying disturbances. This class of SMO-based methods has a fast disturbance tracking rate, but the chattering problem is difficult to completely eliminate. Another idea to address the prediction errors introduced by disturbances is to utilize model-free based methods [23,24]. This approach completely eliminates the dependence on motor parameters by using a generalized estimation method instead of using a motor model. Furthermore, in order to compensate for external disturbances, another study [25] suggests the use of extended state observer (ESO) for the estimation of lumped disturbances. Although the robustness of MPCC is enhanced, the dynamic performance of the motor is limited due to the lack of the model.

In this paper, an ESO-based robust CCS-MPCC is proposed to enhance the dynamic performance and parameter robustness of DTP-PMSM drives. The external disturbances caused by parameter uncertainties or model nonlinearities are considered as lumped disturbances, which are uniformly estimated by ESO and compensated cycle-by-cycle into MPCC, which effectively enhances the anti-disturbance performance of MPCC. The main contributions of this paper are as follows:

(1) The conventional DTP-PMSM mathematical model is modified to a form with disturbance term, and an observer is designed for cycle-by-cycle estimation to enhance the disturbance immunity of the controller.
(2) An observer-based MPCC is constructed where the prediction error of the controller is corrected and compensated by the observer in real time. Additionally, the parameter design method of the observer is given to simplify the design.
(3) By solving the predictive controller explicitly in the forward direction instead of iteratively, the computational resource consumption is not increased significantly considering the extra subspace of the multi-phase motor.

The rest of the paper is organized by the following structure. The mathematical model construction of DTP-PMSM is given in Section 2. The design procedure, as well as the principle of MPCC, is shown in Section 3. The observer compensation based MPCC, as well as the parameter design of the observer, is presented in Section 4. Comparative experimental results are available in Section 5. The discussion and conclusion are given in Section 6.

2. Mathematical Modeling of the Dual Three-Phase Motor

The mathematical electrical model of dual three-phase motor in the natural coordinate system is:

$$\boldsymbol{u}_{6s} = \boldsymbol{R}_{6s}\boldsymbol{i}_{6s} + \frac{d\boldsymbol{\Phi}_{6s}}{dt} \tag{1}$$

where $\boldsymbol{u}_{6s}$ is the motor stator voltage vector, $\boldsymbol{R}_{6s}$ is denoted as the stator resistance diagonal matrix, $\boldsymbol{i}_{6s}$ represents the stator current vector and $\boldsymbol{\Phi}_{6s}$ means the stator magnetic flux vector. It is quite challenging to control the motor directly using model (1). Therefore, the VSD control strategy is employed in this paper, which significantly simplifies the difficulty of control. The VSD-based rotation matrix $\mathbf{T}_{\text{VSD}}$ is represented by:

$$\mathbf{T}_{\text{VSD}} = \frac{1}{3}\begin{bmatrix} 1 & -1/2 & -1/2 & \sqrt{3}/2 & -\sqrt{3}/2 & 0 \\ 0 & \sqrt{3}/2 & -\sqrt{3}/2 & 1/2 & 1/2 & -1 \\ 1 & -1/2 & -1/2 & -\sqrt{3}/2 & \sqrt{3}/2 & 0 \\ 0 & -\sqrt{3}/2 & \sqrt{3}/2 & 1/2 & 1/2 & -1 \end{bmatrix}$$

The mathematical model of the motor is decomposed to α-β subspace and x-y subspace by applying the rotation matrix $\mathbf{T}_{\text{VSD}}$ to model (1). The α-β subspace is used to control the electromechanical energy conversion, while the x-y subspace is used to control the harmonic components of the motor. Further, the α-β subspace is transformed to the d-q subspace via the Park transformation, which enables the control of the alternating current to direct current. As a result, the mathematical model of the motor is expressed as:

$$\begin{cases} u_d(t) = R_s i_d(t) + L_d \dfrac{di_d(t)}{dt} - \omega_{\text{e}}(t)L_q i_q(t) \\ u_q(t) = R_s i_q(t) + L_q \dfrac{di_q(t)}{dt} + \omega_{\text{e}}(t)L_d i_d(t) + \omega_{\text{e}}(t)\phi_{\text{f}} \\ u_x(t) = R_s i_x(t) + L_{xy} \dfrac{di_x(t)}{dt} \\ u_y(t) = R_s i_y(t) + L_{xy} \dfrac{di_y(t)}{dt} \end{cases} \tag{2}$$

where u_d, u_q, u_x and u_y are denoted as voltages under the d-, q-, x- and y-axis, respectively, which are utilized to control the behavior of the motor [V]; i_d, i_q, i_x and i_y are the currents under the d-, q-, x- and y-axis, respectively [A]; R_s is denoted as the stator resistance [Ω]; L_d and L_q are the direct and quadrature axis inductances [H]; L_{xy} is the leakage inductance [H]; ω_{e} is the motor electrical speed [rad s^{-1}] and ϕ_{f} is the magnetic flux of permanent magnets [Wb].

Expressing model (2) as the state space expression, one can obtain the mathematical control model as follows:

$$\begin{cases} \dot{\boldsymbol{x}}(t) = \mathbf{A}_{\text{c}}\boldsymbol{x}(t) + \mathbf{B}_{u\text{c}}\boldsymbol{u}(t) + \mathbf{B}_{d\text{c}}\boldsymbol{d}(t) \\ \boldsymbol{y}(t) = \mathbf{C}_{\text{c}}\boldsymbol{x}(t) \end{cases} \tag{3}$$

where $\boldsymbol{x} = [i_d, i_q, i_x, i_y]^{\text{T}}$ is the state variable; $\boldsymbol{u} = [u_d, u_q, u_x, u_y]^{\text{T}}$ is the control effort; $\boldsymbol{d} = \omega_{\text{e}}$ is the measurable disturbance and $\boldsymbol{y} = [i_d, i_q, i_x, i_y]^{\text{T}}$ is the system output. $\mathbf{A}_{\text{c}}$ and $\mathbf{B}_{u\text{c}}$ are given by (4); $\mathbf{B}_{d\text{c}} = \text{diag}[0, \phi_f/L_q, 0, 0]^{\text{T}}$ and $\mathbf{C}_{\text{c}} = \mathbf{I}$ is a unit matrix.

$$\mathbf{A}_{\text{c}} = \begin{bmatrix} -\dfrac{R_s}{L_d} & \dfrac{\omega_{\text{e}}L_q}{L_d} & 0 & 0 \\ -\dfrac{\omega_{\text{e}}L_d}{L_q} & -\dfrac{R_s}{L_d} & 0 & 0 \\ 0 & 0 & -\dfrac{R_s}{L_{xy}} & 0 \\ 0 & 0 & 0 & -\dfrac{R_s}{L_{xy}} \end{bmatrix}, \mathbf{B}_{d\text{c}} = \begin{bmatrix} \dfrac{1}{L_d} & 0 & 0 & 0 \\ 0 & \dfrac{1}{L_q} & 0 & 0 \\ 0 & 0 & \dfrac{1}{L_{xy}} & 0 \\ 0 & 0 & 0 & \dfrac{1}{L_{xy}} \end{bmatrix} \tag{4}$$

Four conventional PI controllers are then applied to control the four current components in x, thereby realizing the decoupled control of the dual three-phase motor. Therefore, the brief principle of conventional motor control is shown in Figure 1.
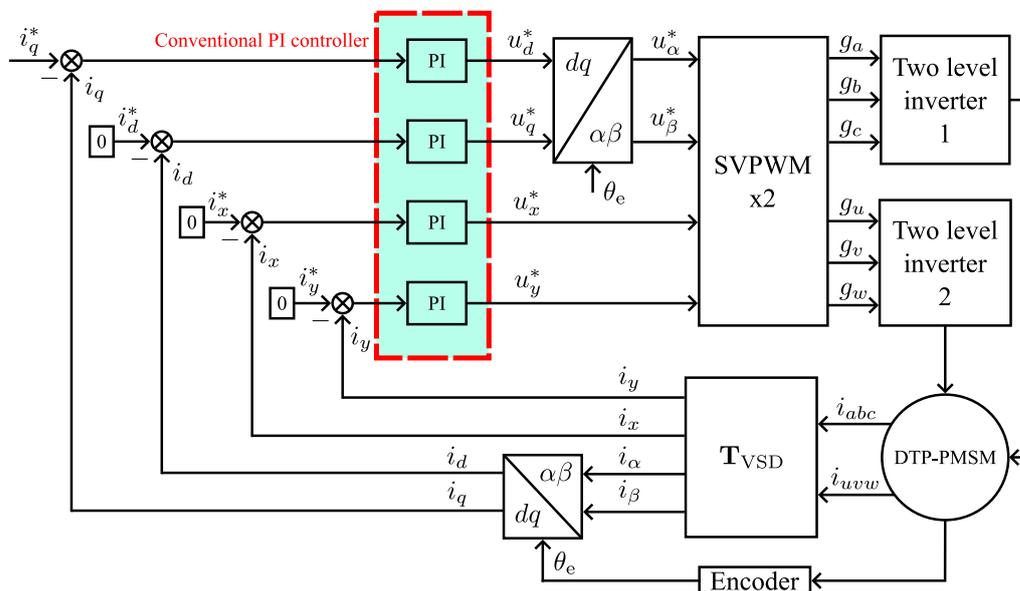
Figure 1. Conventional VSD control method for DTP-PMSM with PI controller.

3. Design of Model Predictive Current Controller

After discretizing model (3) with the first-order Euler discretization method, the prediction model used for the controller is obtained as:

$$\begin{cases} x(k+1) = \mathbf{A}x(k) + \mathbf{B}_u u(k) + \mathbf{B}_d d(t) \\ y(k) = \mathbf{C}x(k) \end{cases} \tag{5}$$

where $\mathbf{A} = T_s\mathbf{A}_c + \mathbf{I}$, $\mathbf{B}_u = T_s\mathbf{B}_{uc}$, $\mathbf{B}_d = T_s\mathbf{B}_{dc}$, $\mathbf{C} = \mathbf{C}_c$ and T_s is sampling period or control period.

In order to achieve the tracking control of the current, the cost function at time step k as shown in Equation (6) is defined.

$$J(k) = \sum_{i=1}^{N_p} \|y(k+i|k) - r(k)\|^2_{\mathbf{\Gamma}_i} \tag{6}$$

where N_p is the prediction horizon and $r = [i_d^*, i_q^*, i_x^*, i_y^*]^T$ is the reference value of current; $y(k+i|k)$ represents the output of the system at step k when the system is predicted to step i; $\mathbf{\Gamma}_i$ is the weight matrix assigned to the different currents in the tracking control at the step k of the prediction. The goal of tracking control is to control the actual current to be consistent with the reference. Therefore, when $J(k)$ in the cost function (6) is smaller, it indicates that the control effort is more effective at the kth step.

Since the electrical constant of the motor is much smaller than the mechanical constant, the measurable disturbance $d(k)$, also referred as the electrical speed, remains constant during the prediction process. Thus, the assumption (7) is satisfied in this paper.

$$d(k) = d(k+1) = \ldots = d(k+N_p) \tag{7}$$

Bringing model (5) and assumption (7) into $y(k+i|k)$, the output of the system $\mathbf{Y}_p(k+1|k) = [y^T(k+1|k), y^T(k+2|k), \ldots, y^T(k+N_u|k), \ldots, y^T(k+N_p|k)]^T$ during the prediction process is derived in (8) and N_u is the control horizon.

$$\mathbf{Y}_{\mathrm{p}}(k+1|k) = \overbrace{\begin{bmatrix} \mathbf{CA} \\ \mathbf{CA}^2 \\ \vdots \\ \mathbf{CA}^{N_{\mathrm{P}}} \end{bmatrix}}^{\mathcal{S}_x} x(k) + \overbrace{\begin{bmatrix} \mathbf{CB}_u & \mathbf{0} & \cdots & \mathbf{0} \\ \mathbf{CAB}_u & \mathbf{CB}_u & \cdots & \mathbf{0} \\ \vdots & \vdots & \ddots & \vdots \\ \mathbf{CA}^{N_{\mathrm{P}}-1}\mathbf{B}_u & \mathbf{CA}^{N_{\mathrm{P}}-2}\mathbf{B}_u & \cdots & \sum_{i=0}^{N_{\mathrm{P}}-N_{\mathrm{u}}}\mathbf{CA}^i\mathbf{B}_u \end{bmatrix}}^{\mathcal{S}_u} \overbrace{\begin{bmatrix} u(k) \\ u(k+1) \\ \vdots \\ u(k+N_{\mathrm{P}}-1) \end{bmatrix}}^{\mathcal{U}(k)}$$

$$+ \overbrace{\begin{bmatrix} \mathbf{CB}_d \\ \mathbf{CAB}_d + \mathbf{CB}_d \\ \vdots \\ \sum_{i=0}^{N_{\mathrm{u}}-1}\mathbf{CA}^i\mathbf{B}_d \end{bmatrix}}^{\mathcal{S}_d} d(k) = \mathcal{S}_x x(k) + \mathcal{S}_u \mathcal{U}(k) + \mathcal{S}_d d(k) \tag{8}$$

The cost function can be further expanded as follows:

$$\begin{aligned}
J(k) &= \sum_{i=1}^{N_{\mathrm{P}}} \|y(k+i|k) - r(k)\|_{\mathbf{\Gamma}_i}^2 \\
&= (\mathbf{Y}_{\mathrm{p}}(k+1|k) - \mathbf{I}_r r(k))^{\mathrm{T}} \overbrace{\mathrm{diag}(\mathbf{\Gamma}_1, \mathbf{\Gamma}_2, \dots, \mathbf{\Gamma}_{N_{\mathrm{P}}})}^{\mathbf{\Gamma}} (\mathbf{Y}_{\mathrm{p}}(k+1|k) - \mathbf{I}_r r(k)) \\
&= (\mathbf{Y}_{\mathrm{p}}(k+1|k) - \mathbf{I}_r r(k))^{\mathrm{T}} (\sqrt{\mathbf{\Gamma}})^{\mathrm{T}} \sqrt{\mathbf{\Gamma}} (\mathbf{Y}_{\mathrm{p}}(k+1|k) - \mathbf{I}_r r(k)) \\
&= (\sqrt{\mathbf{\Gamma}}\mathbf{Y}_{\mathrm{p}}(k+1|k) - \sqrt{\mathbf{\Gamma}}\mathbf{I}_r r(k))^{\mathrm{T}} (\sqrt{\mathbf{\Gamma}}\mathbf{Y}_{\mathrm{p}}(k+1|k) - \sqrt{\mathbf{\Gamma}}\mathbf{I}_r r(k))
\end{aligned} \tag{9}$$

where $\mathbf{I}_r = [\mathbf{I}, \mathbf{I}, \dots, \mathbf{I}]^{\mathrm{T}}$ and $\mathbf{\Gamma}_i$ denotes the diagonal matrix of weighting coefficients assigned to the different current components in the tracking control at prediction step i. Substituting (8) into (9), $J(k)$ is simplified to:

$$J(k) = (\mathbf{MX} - \mathbf{N})^{\mathrm{T}}(\mathbf{MX} - \mathbf{N}) \tag{10}$$

and:

$$\mathbf{M} = \sqrt{\mathbf{\Gamma}}\mathcal{S}_u, \ \mathbf{X} = \mathcal{U}(k), \ \mathbf{N} = \sqrt{\mathbf{\Gamma}}(\mathbf{I}_r r(k) - \mathcal{S}_x x(k) - \mathcal{S}_d d(k)) \tag{11}$$

By taking the partial derivative of (10) and making it zero, the optimal control effort $\mathcal{U}^*(k)$ at step k is found.

$$\frac{\partial J(k)}{\partial \mathbf{X}} = 0 \Rightarrow \mathbf{X}^* = \mathcal{U}^*(k) = (\mathbf{M}^{\mathrm{T}}\mathbf{M})^{-1}\mathbf{M}^{\mathrm{T}}\mathbf{N} \tag{12}$$

Considering that only the first step control effort is applied, the control output at step k is:

$$\begin{aligned}
u^*(k) &= [\mathbf{I}, \mathbf{0}, \dots, \mathbf{0}]\mathcal{U}^*(k) \\
&= [\mathbf{I}, \mathbf{0}, \dots, \mathbf{0}]\overbrace{(\mathcal{S}_u^{\mathrm{T}}(\sqrt{\mathbf{\Gamma}})^{\mathrm{T}}\sqrt{\mathbf{\Gamma}}\mathcal{S}_u)^{-1}\mathcal{S}_u^{\mathrm{T}}(\sqrt{\mathbf{\Gamma}})^{\mathrm{T}}\sqrt{\mathbf{\Gamma}}}^{\mathbf{K}_{\mathrm{mpc}}}(\mathbf{I}_r r(k) - \mathcal{S}_x x(k) - \mathcal{S}_d d(k)) \\
&= \mathbf{K}_{\mathrm{mpc}}(\mathbf{I}_r r(k) - \mathcal{S}_x x(k) - \mathcal{S}_d d(k))
\end{aligned} \tag{13}$$

Consequently, the controller (13) is the ideal model predictive current controller, and the optimal control output is applied to the inverter at each control cycle.

4. Proposed Observer-Based Robust MPCC Method

Due to unavoidable parameter uncertainties or model nonlinearities such as inverter dead-time, the prediction error occurs when model (3) is used to predict the current, resulting in deterioration of the control performance. Therefore, an observer-based predictive current controller is proposed in this section.

4.1. Observer-Based Predictive Controller Design

The ideal prediction model (3) is adapted to correct the prediction error as shown in model (14). Compared to the existing models, model (14) possesses the capability of disturbance correction, which achieves better accuracy in prediction.

$$\begin{cases} \dot{x}(t) = \mathbf{A}_c x(t) + \mathbf{B}_{uc} u(t) + \mathbf{B}_{dc} d(t) + \mathbf{B}_{fc} f(t) \\ y(t) = \mathbf{C}_c x(t) \end{cases} \tag{14}$$

where $\mathbf{B}_{fc} = \mathbf{I}$ is a unit matrix; $f(t)$ is the external lumped disturbance and requires to be estimated in real time. Taking the motor parameters from Table 1 into the observability matrix of the system, the rank of the matrix is 4 as shown in (15), which is consistent with the system dimension. Therefore, the system is observable.

$$\text{rank} \left(\begin{bmatrix} \mathbf{C}_c \\ \mathbf{C}_c \mathbf{A}_c \\ \mathbf{C}_c \mathbf{A}_c^2 \\ \mathbf{C}_c \mathbf{A}_c^3 \end{bmatrix} \right) = 4 = \text{dimension of the system} \tag{15}$$

Table 1. Parameters of the DTP-PMSM used for verification.

Parameters	Symbols	Value	Unit
Rated voltage	U_{dc}	48	V
Rated current	I_r	4.67	A_{rms}
Pole pairs	p	5	-
Resistance	R_s	0.188	Ω
D-axis inductance	L_d	0.366	mH
Q-axis inductance	L_q	0.366	mH
Leakage inductance	L_{xy}	0.137	mH
Magnetic flux linkage	ϕ_f	6.678	mWb

The ESO based on model (14) is constructed to estimate $f(t)$ cycle-by-cycle as follows:

$$\begin{cases} \dot{\hat{z}}(t) = (\widetilde{\mathbf{A}}_c - \mathbf{L}_c \widetilde{\mathbf{C}}_c) \hat{z}(t) + \widetilde{\mathbf{B}}_{uc} u(t) + \widetilde{\mathbf{B}}_{dc} d(t) + \mathbf{L}_c \mathbf{C}_c x(t) \\ \hat{y}(t) = \widetilde{\mathbf{C}}_c \hat{z}(t) \end{cases} \tag{16}$$

where $z(t) = [x^T(t), f^T(t)]^T$ and $\hat{z}(t)$ is the estimation of $z(t)$; $\widetilde{\mathbf{A}}_c$, $\mathbf{L}_c$, $\widetilde{\mathbf{C}}_c$, $\widetilde{\mathbf{B}}_{uc}$ and $\widetilde{\mathbf{B}}_{dc}$ are given by (17). The design of the observer gain $\mathbf{L}_c$ will be presented in the following Section 4.2.

$$\widetilde{\mathbf{A}}_c = \begin{bmatrix} \mathbf{A}_c & \mathbf{B}_{fc} \\ \mathbf{0} & \mathbf{0} \end{bmatrix}, \ \mathbf{L}_c = \begin{bmatrix} \mathbf{L}_{c1} \\ \mathbf{L}_{c2} \end{bmatrix}, \ \widetilde{\mathbf{C}}_c = \begin{bmatrix} \mathbf{C}_c & \mathbf{0} \end{bmatrix}, \ \widetilde{\mathbf{B}}_{uc} = \begin{bmatrix} \mathbf{B}_{uc} \\ \mathbf{0} \end{bmatrix}, \ \widetilde{\mathbf{B}}_{dc} = \begin{bmatrix} \mathbf{B}_{dc} \\ \mathbf{0} \end{bmatrix},$$

$$\mathbf{L}_{c1} = \text{diag}(\beta_d, \beta_q, \beta_x, \beta_y), \ \mathbf{L}_{c2} = \text{diag}(\beta_{fd}, \beta_{fq}, \beta_{fx}, \beta_{fy}) \tag{17}$$

By discretizing the observer (16) with first-order Euler discretization, the lumped disturbance estimation $\hat{f}$ of the model is estimated with (18). The disturbances are used to compensate for model uncertainties or nonlinearities in the prediction process, thus improving the robustness of the controller.

$$\begin{cases} \hat{x}(k+1) = (\mathbf{A} - T_s \mathbf{L}_{c1} \mathbf{C}) \hat{x}(k) + \mathbf{B}_f \hat{f}(k) + \mathbf{B}_u u(k) + \mathbf{B}_d d(k) + T_s \mathbf{L}_{c1} \mathbf{C} x(k) \\ \hat{f}(k+1) = -T_s \mathbf{L}_{c2} \mathbf{C} \hat{x}(k) + \hat{f}(k) + T_s \mathbf{L}_{c2} \mathbf{C} x(k) \end{cases} \tag{18}$$

When the model (14) is utilized for prediction, the optimal controller in Section 3 can be derived and modified in a similar way, as seen below:

$$u^*(k) = \mathbf{K}_{\mathrm{mpc}}(\mathbf{I_r}r(k) - \mathcal{S}_x x(k) - \mathcal{S}_d d(k) - \mathcal{S}_f f(k)), \; \mathcal{S}_f = \begin{bmatrix} \mathbf{C}T_s\mathbf{B}_{fc} \\ \mathbf{C}T_s\mathbf{B}_{fc} + \mathbf{C}T_s\mathbf{B}_{fc} \\ \vdots \\ \sum_{i=0}^{N_u-1} \mathbf{C}\mathbf{A}^i T_s\mathbf{B}_{fc} \end{bmatrix} \quad (19)$$

Substituting the estimation results of the observer (18) into the predictive controller (19), the ESO-based robust MPCC is designed.

$$u^*(k) = \mathbf{K}_{\mathrm{mpc}}(\mathbf{I_r}r(k) - \mathcal{S}_x \hat{x}(k) - \mathcal{S}_d d(k) - \mathcal{S}_f \hat{f}(k)) \quad (20)$$

Further, when considering one-step delay of the digital system, the current x and the disturbance f require to be predicted one step before being brought into the controller. Therefore, Equation (20) is modified:

$$u^*(k+1) = \mathbf{K}_{\mathrm{mpc}}(\mathbf{I_r}r(k) - \mathcal{S}_x \hat{x}(k+1) - \mathcal{S}_d d(k) - \mathcal{S}_f \hat{f}(k+1)) \quad (21)$$

Finally, the logic schematic of the proposed method is presented in Figure 2. The disturbances are estimated and compensated into the controller in real time, which effectively improves the robustness of the proposed method to parameter inaccuracies as well as the dynamic performance.
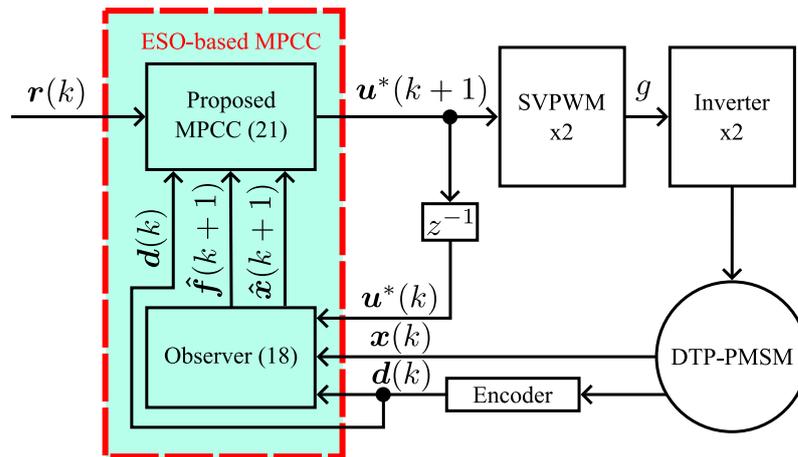
Figure 2. The schematic description of proposed ESO-based robust MPCC.

4.2. Parameter Design of the Observer

In order to guarantee stability, the eigenvalues of the system matrix $\widetilde{\mathbf{A}}_c - \mathbf{L}_c\widetilde{\mathbf{C}}_c$ in the observer (16) should have a negative real part. Therefore, the pole placement method is adopted for designing the parameters of the observer.

$$\left| s\mathbf{I} - (\widetilde{\mathbf{A}}_c - \mathbf{L}_c\widetilde{\mathbf{C}}_c) \right| = (s + \omega_{\mathrm{ob}})^8 \quad (22)$$

where s is the Laplace operator and ω_{ob} is the desired bandwidth of the observer. Larger bandwidth brings faster observation speeds. However, this is a tradeoff between speed and noise amplification, which introduces instability as well as vibration into the system.

By solving (22), the parameters of the observer are derived as follows:

$$\begin{cases} \beta_d = 2\omega_{\mathrm{ob}} - \dfrac{R_s}{L_d} - \omega_e \\[2mm] \beta_q = 2\omega_{\mathrm{ob}} - \dfrac{R_s}{L_q} + \omega_e \\[2mm] \beta_x = \beta_y = 2\omega_{\mathrm{ob}} - \dfrac{R_s}{L_{xy}} \\[2mm] \beta_{fd} = \beta_{fq} = \beta_{fx} = \beta_{fy} = \omega_{\mathrm{ob}}^2 \end{cases} \quad \text{or} \quad \begin{cases} \beta_d = 2\omega_{\mathrm{ob}} - \dfrac{R_s}{L_d} + \omega_e \\[2mm] \beta_q = 2\omega_{\mathrm{ob}} - \dfrac{R_s}{L_q} - \omega_e \\[2mm] \beta_x = \beta_y = 2\omega_{\mathrm{ob}} - \dfrac{R_s}{L_{xy}} \\[2mm] \beta_{fd} = \beta_{fq} = \beta_{fx} = \beta_{fy} = \omega_{\mathrm{ob}}^2 \end{cases} \quad (23)$$

5. Experimental Results

In order to verify the effectiveness of the proposed method, multiple sets of experiments are implemented. In addition, the conventional PI control method is realized for comparison of performance. The controllers are all run in the TMS320F28388D (digital signal processor) manufactured by Texas Instruments. In addition, the DTP-PMSM is mounted on the testbench, and the simulated load is provided by a load motor. The parameters of the DTP-PMSM are listed in Table 1 and the whole experimental platform is shown in Figure 3.
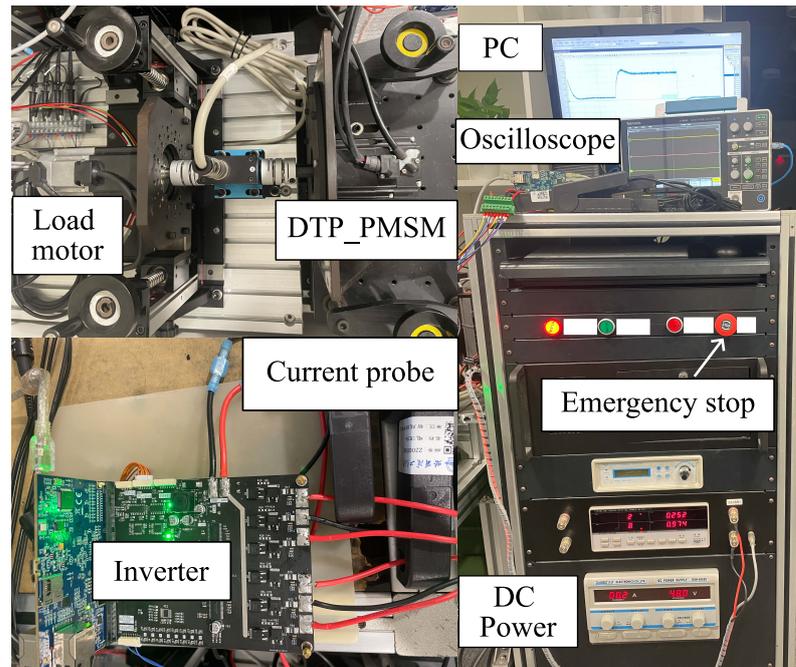
Figure 3. The testbench used for experimental validation.

The parameters of the proposed method are listed in Table 2. Considering the computational complexity, N_p and N_u are determined as 2 and 1, respectively, to simplify the computation. At the same time, the desired bandwidth of observer ω_{ob} is selected as 500 Hz to satisfy the fast observation performance without signal noise amplification. In addition, $\boldsymbol{\Gamma}$ is chosen as a unit matrix due to the same importance of tracking control for different currents. Additionally, the parameters of proportional coefficient K_p and integral coefficient K_i with conventional PI control are calculated by Equation (24), where ω_{PI} is the desired bandwidth.

$$\begin{cases} K_P = \omega_{PI} L_{d(q)} \\ K_i = \dfrac{R_s}{L_{d(q)}} \end{cases} \tag{24}$$

Table 2. Parameters of proposed method.

Parameters	N_p	N_u	ω_{ob}	$\boldsymbol{\Gamma}$	T_s
Value	2	1	500 Hz	$\mathbf{I}$	100 µs

5.1. Dynamic Experimental Results with Speed Reversal

The speed reversal experiments are implemented to verify the dynamic performance of the proposed method during speed variation. The test motor is operated in speed loop, and the speed reference of the motor is changed abruptly from -1500 RPM to 1500 RPM at 40 ms.

Figure 4 presents the experimental results of the a-phase current i_a, the reference and actual values of the current in the q-axis, and the mechanical speed ω_m when the motor is

reversed. The figure shows that the tracking performance of the q-axis current suffers from a large latency and a steady state error when using a conventional PI controller, while the proposed method demonstrates a better satisfactory tracking performance and eliminates the steady state error. In addition, the settling time of the speed is reduced from 138 ms with the PI controller to 74 ms with the proposed method, which further validates the effectiveness of the proposed method.

(**a**)   (**b**)
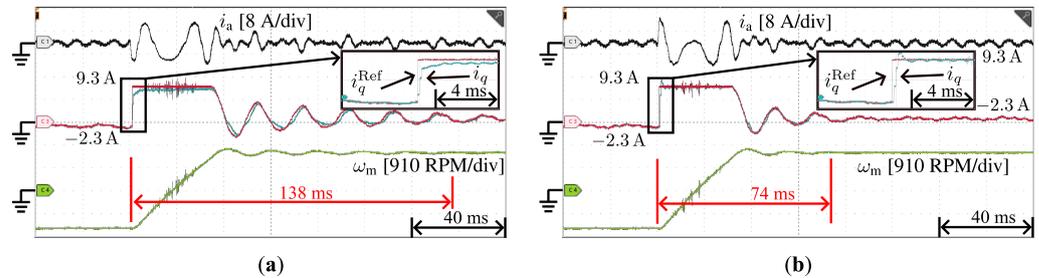
Figure 4. Experimental results of a-phase currents i_a, actual and reference values of q-axis currents, mechanical speed ω_m when the mechanical reference speed changes abruptly from -1500 RPM to 1500 RPM at 40 ms using different controllers. (**a**) PI controller (**b**) Proposed method.

Figure 5 demonstrates the d-axis current tracking results when the speed is reversed. It is clear from the figure that the PI controller has an overshoot of -1.86 A at 40 ms, with a noticeable ripple following. The proposed method has only a current overshoot of -0.88 A, and the steady state ripple is significantly lower than that of the conventional method. Additionally, in order to evaluate the tracking performance of the currents properly, the root-mean-square (RMS) value of the tracking error is employed for the comparison. As shown in Figure 6, the RMS values of the d-axis and q-axis current following error with the PI controller are 0.26 A and 0.51 A, respectively, while the proposed method has a following error RMS value of 0.07 A and 0.38 A, which is significantly improved over the conventional method.
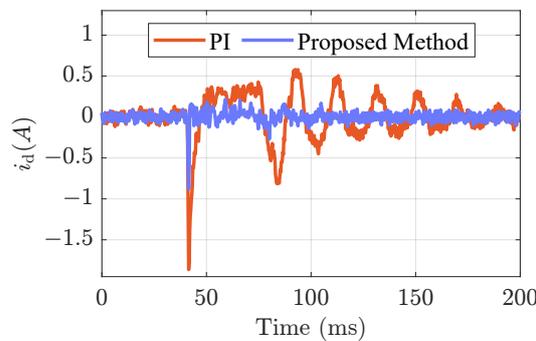
Figure 5. Experimental results of d-axis current tracking performance when the mechanical reference speed changes abruptly from -1500 RPM to 1500 RPM at 40 ms.
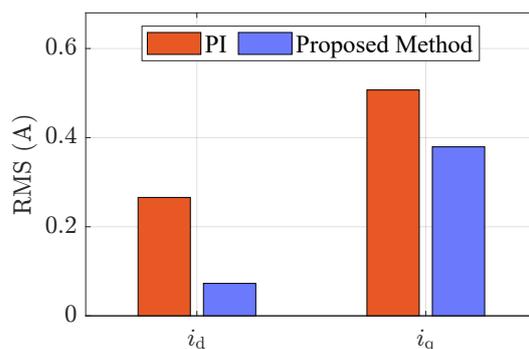
Figure 6. Experimental results of RMS for d-axis and q-axis current following errors with different controllers when the mechanical reference speed changes abruptly from -1500 RPM to 1500 RPM.

5.2. Dynamic Experimental Results with Load Disturbance

To verify the dynamic performance of the proposed method under load disturbance, the conventional and the proposed method are implemented for comparison. The test motor operates in speed loop mode, and the reference value of speed is set to 1500 RPM, while the load motor operates in current loop mode and is connected to the test motor through mechanical coupling to provide simulated load disturbance. At the time of 20 ms, the torque of the load motor is set to the rated value.

Figure 7 shows the dynamic experimental results of different controllers under load disturbance. The figure shows that the PI controller has a maximum speed drop of 191 RPM with a settling time of 20 ms under load disturbance, while the proposed method has a maximum speed drop of 189 RPM with a settling time of 21 ms, which indicates that the proposed method has similar performance to the conventional controller. However, Figure 8 shows that for the d-axis current tracking performance, the conventional PI controller has a large current overshoot of 0.79 A. The proposed method eliminates this overshoot, and the maximum overshoot is only 0.10 A, which demonstrates that the proposed method can provide satisfactory current tracking performance, especially for the d-axis current during the load vibration.
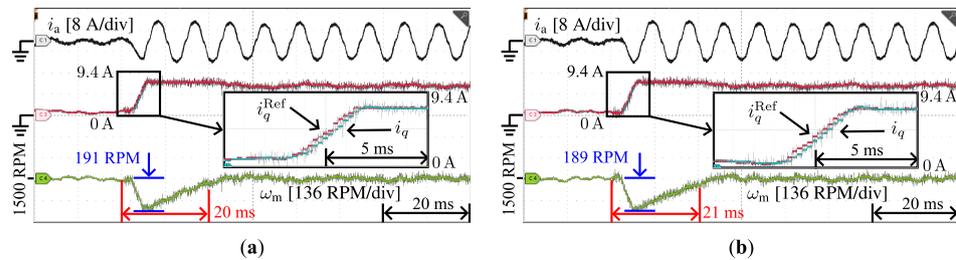
Figure 7. Experimental results of a-phase currents i_a, actual and reference values of q-axis currents, mechanical speed ω_m when the load changes abruptly from no load to rated load at 20 ms using different controllers. (**a**) PI controller (**b**) Proposed method.
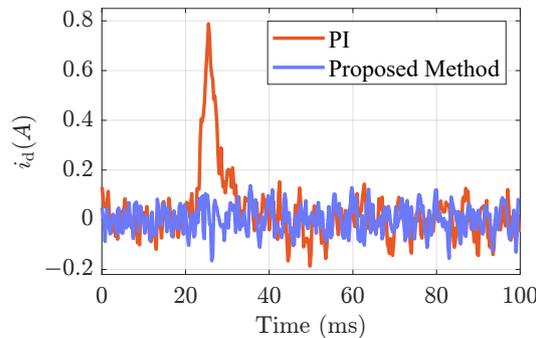
Figure 8. Experimental results of d-axis current tracking performance when the load changes abruptly from no load to rated load at 20 ms.

In addition, the RMS results of the d-axis and q-axis current following errors are presented in Figure 9. For the q-axis current, the RMS of the following errors with the conventional method and the proposed method is 0.12 A and 0.12 A, respectively, which are quite similar. Nevertheless, for the following error of the d-axis current, the RMS values are 0.13 A and 0.06 A, respectively. This indicates that the proposed method provides more efficient performance for d-axis current tracking.
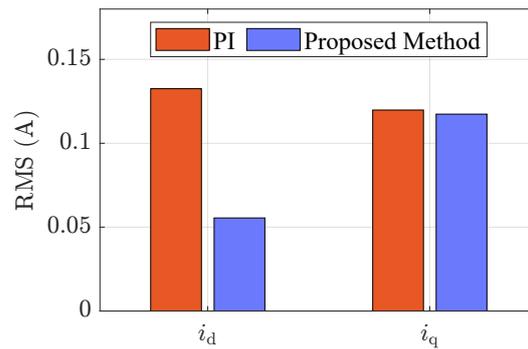
Figure 9. Experimental results of RMS for d-axis and q-axis current following errors with different controllers when the load changes abruptly from no load to rated load.

5.3. Experimental Results on Parameter Robustness

This set of experiments demonstrates the robust current tracking control performance of the PI controller and proposed method under different motor parameters. The test conditions are the same as in Section 5.1, where the test motor is operated in the speed loop mode, and the speed reference is changed abruptly from -1500 RPM to 1500 RPM.

As can be seen from Table 3, the current following error RMS values of the proposed method under nominal motor parameters are 0.07 A for i_d and 0.37 A for i_q. As the variation in the motor parameters, the following error RMS values of the d-axis currents remain at 0.06 A to 0.18 A. At the same time, the following error RMS values of the q-axis current present a minor difference with the variation in the parameters. Even the worst case, i.e., at 50 % of $L_d(L_q)$, is still 0.55 A, which is only a slight performance degradation compared to 0.37 A at the nominal parameter. This indicates that the proposed method has satisfactory robust current control performance for motor parameter variations.

Table 3. Experimental results of robust current tracking control with the proposed method under different motor parameter conditions when the mechanical reference speed changes abruptly from -1500 RPM to 1500 RPM.

Methods	Conditions	RMS (A)	
		i_d	i_q
PI	Nominal	0.28	0.53
Proposed method		**0.07**	**0.37**
PI	50%R_s	0.32	0.70
Proposed method		**0.06**	**0.37**
PI	150%R_s	0.21	0.47
Proposed method		**0.08**	**0.37**
PI	50%L_d (L_q)	0.42	0.81
Proposed method		**0.18**	**0.55**
PI	150%L_d (L_q)	0.20	0.45
Proposed method		**0.06**	**0.33**

5.4. Experimental Results of Frequency Response

For further investigation into the dynamic performance of the proposed method, frequency response experiments of both PI and the proposed controller are realized. The load motor is removed from the mechanical coupling since free rotation is required for the test motor. Additionally, a sinusoidal signal with an amplitude of 1.85 A and a frequency from 2 Hz to 2975 Hz is injected into the q-axis current of the test motor. By collecting the response results of the current and analyzing them in comparison with the injected signal, one can obtain the closed-loop frequency response plot of the system, as shown in Figure 10. The figure shows that the closed-loop bandwidth of the conventional PI method

has only 387 rad s^{-1}, while the proposed method increases the bandwidth to 1839 rad s^{-1}. Therefore, the proposed method effectively increases the bandwidth of the closed-loop system and offers sufficient current tracking capability.
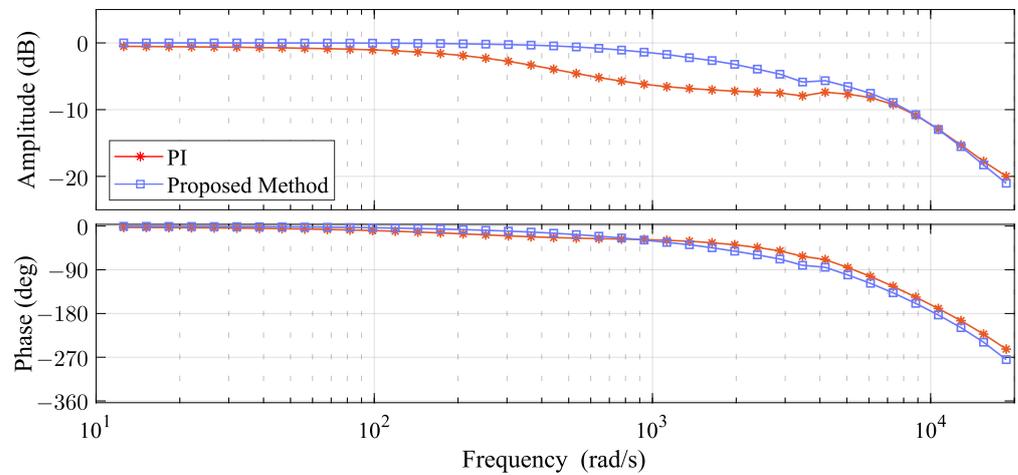
Figure 10. Experimental results of frequency response for q-axis current with different controllers.

5.5. Experimental Results on Computational Burden

Predictive controllers are often known for having significant computational burdens; therefore, the computational time consumed by different controllers is evaluated. By toggling the output port before and after the controller operation, the running time of PI and proposed controller are measured by an oscilloscope as shown in Figure 11. The longer the computation time, the more resources the method consumes. From the figure, it is clear that the computational time consumed by the conventional PI controller is 14 μs while the proposed method consumes 17 μs, which is not a significant increase in time. This is because the predictive controller used in the proposed method directly computes the optimal control result without iterative solving or searching for all the available voltage vectors.

Figure 11. Experimental results of computational time consumption with different controls. (**a**) PI controller (**b**) Proposed method.

Regardless of which controller is used, there is sufficient remaining time to execute other control algorithms, such as position loop or vibration suppression, compared to a control cycle of 100 μs. Therefore, the proposed method provides better control performance without significant consumption of computational resources.

6. Discussion and Conclusions

In this paper, an extended state observer-based model predictive current controller is proposed for DTP-PMSM drives to improve the dynamic performance of the current loop. The mathematical model of the motor is briefly derived and discretized for predicting the current. In addition, the multi-step continuous control set predictive controller is derived and given to obtain an explicit solution for the optimal control voltage, which does not

introduce a significant increase in computation time. In order to address the performance deterioration due to prediction errors, a robust observer-based MPCC method is designed for efficient observation of external disturbances, and the parameter design methodology of the observer is also presented. At each control period, external disturbances due to factors such as parameter inaccuracies or nonlinearities in the model are observed. At the same time, the observation results are compensated into the controller in real time after a step of prediction, which is applied to correct the prediction error. Therefore, the proposed method improves the dynamic performance and robustness to external disturbances effectively. Finally, multiple sets of experimental results are demonstrated to indicate the effectiveness of the proposed method.

Since the proposed method is based on a generalized motor model and the external disturbances are uniformly observed without loss of generality, it can be applied to DTP-PMSM at various power levels, including low-power applications, such as robotic arm joint motors or quadruped robots and high-power applications, such as electric vehicles, power trains, and other fields. As the external disturbances are uniformly observed in this study, future work can physically model some of the disturbances to reduce the observation requirements of the observer and further enhance the robust performance of the controller.

References

1. Wu, Z.; Cheng, C.; Hua, W.; Zhang, H.; Yin, H.; Hu, M. A Sensorless Control Method Based on High Frequency Injection for Dual Three Phase Motor with Asymmetric Windings. In Proceedings of the 2022 25th International Conference on Electrical Machines and Systems (ICEMS), Chiang Mai, Thailand, 29 November–2 December 2022; pp. 1–6. [CrossRef]
2. Miyama, Y.; Ishizuka, M.; Kometani, H.; Akatsu, K. Vibration Reduction by Applying Carrier Phase-Shift PWM on Dual Three-Phase Winding Permanent Magnet Synchronous Motor. *IEEE Trans. Ind. Appl.* **2018**, *54*, 5998–6004. [CrossRef]
3. Yu, K.; Wang, Z. An Online Compensation Method of VSI Nonlinearity for Dual Three-Phase PMSM Drives Using Current Injection. *IEEE Trans. Power Electron.* **2022**, *37*, 3769–3774. [CrossRef]
4. Huang, Y.; Walden, J.; Zhang, X.; Yan, Y.; Bai, H.; Jin, F.; Cheng, B. A Novel Zero/Reduced Common-Mode Voltage Modulation Scheme for a Dual Three-Phase Motor Drive System in Full Modulation Span. *IEEE Trans. Power Electron.* **2022**, *37*, 6765–6779. [CrossRef]
5. Amin, M.M.; El-Sousy, F.F.M.; Mohammed, O.A.; Aziz, G.A.A.; Gaber, K. MRAS-Based Super-Twisting Sliding-Mode Estimator Combined With Block Control and DTC of Six-Phase Induction Motor for Ship Propulsion Application. *IEEE Trans. Ind. Appl.* **2021**, *57*, 6646–6658. [CrossRef]
6. Nair, S.V.; Harikrishnan, P.; Hatua, K. Six-Step Operation of a Symmetric Dual Three-Phase PMSM With Minimal Circulating Currents for Extended Speed Range in Electric Vehicles. *IEEE Trans. Ind. Electron.* **2022**, *69*, 7651–7662. [CrossRef]
7. Zhang, Z.; Sun, Q.; Zhang, Q. A Computationally Efficient Model Predictive Control Method for Dual Three-Phase PMSM of Electric Vehicle With Fixed Switching Frequency. *IEEE Trans. Ind. Appl.* **2023**, *early access*. [CrossRef]
8. Chen, Z.; Shi, T.; Lin, Z.; Wang, Z.; Gu, X. Analysis and Control of Current Harmonic in IPMSM Field-Oriented Control System. *IEEE Trans. Power Electron.* **2022**, *37*, 9571–9585. [CrossRef]
9. Zhao, Y.; Lipo, T. Space vector PWM control of dual three-phase induction machine using vector space decomposition. *IEEE Trans. Ind. Appl.* **1995**, *31*, 1100–1109. [CrossRef]
10. Carlet, P.G.; Favato, A.; Bolognani, S.; Dörfler, F. Data-Driven Continuous-Set Predictive Current Control for Synchronous Motor Drives. *IEEE Trans. Power Electron.* **2022**, *37*, 6637–6646. [CrossRef]
11. Zhang, Y.; Yin, Z.; Li, W.; Liu, J.; Zhang, Y. Adaptive Sliding-Mode-Based Speed Control in Finite Control Set Model Predictive Torque Control for Induction Motors. *IEEE Trans. Power Electron.* **2021**, *36*, 8076–8087. [CrossRef]
12. Mousavi, M.S.; Davari, S.A.; Nekoukar, V.; Garcia, C.; Rodriguez, J. Computationally Efficient Model-Free Predictive Control of Zero-Sequence Current in Dual Inverter Fed Induction Motor. *IEEE J. Emerg. Sel. Top. Power Electron.* **2023**, *11*, 1332–1344. [CrossRef]

13.　Jiang, X.; Yang, Y.; Fan, M.; Ji, A.; Xiao, Y.; Zhang, X.; Zhang, W.; Garcia, C.; Vazquez, S.; Rodriguez, J. An Improved Implicit Model Predictive Current Control With Continuous Control Set for PMSM Drives. *IEEE Trans. Transport. Electr.* **2022**, *8*, 2444–2455. [CrossRef]

14.　Liu, S.; Liu, C. Virtual-Vector-Based Robust Predictive Current Control for Dual Three-Phase PMSM. *IEEE Trans. Ind. Electron.* **2021**, *68*, 2048–2058. [CrossRef]

15.　Zhang, Z.; Wang, Z.; Wei, X.; Liang, Z.; Kennel, R.; Rodriguez, J. Space-Vector-Optimized Predictive Control for Dual Three-Phase PMSM With Quick Current Response. *IEEE Trans. Power Electron.* **2022**, *37*, 4453–4462. [CrossRef]

16.　Lim, C.S.; Lee, S.S.; Levi, E. Continuous-Control-Set Model Predictive Current Control of Asymmetrical Six-Phase Drives Considering System Nonidealities. *IEEE Trans. Ind. Electron.* **2023**, *70*, 7615–7626. [CrossRef]

17.　Alfaro, C.; Guzman, R.; de Vicuña, L.G.; Miret, J.; Castilla, M. Dual-Loop Continuous Control Set Model-Predictive Control for a Three-Phase Unity Power Factor Rectifier. *IEEE Trans. Power Electron.* **2022**, *37*, 1447–1460. [CrossRef]

18.　Wang, T.; Guo, L.; Wang, K.; Wu, J.; Liu, C.; Zhu, Z. Generalized Predictive Current Control for Dual-Three-Phase PMSM to Achieve Torque Enhancement Through Harmonic Injection. *IEEE Trans. Power Electron.* **2023**, *38*, 6422–6433. [CrossRef]

19.　Wang, X.; Wang, Z.; Xu, Z.; Wang, W.; Wang, B.; Zou, Z. Deadbeat Predictive Current Control-Based Fault-Tolerant Scheme for Dual Three-Phase PMSM Drives. *IEEE J. Emerg. Sel. Top. Power Electron.* **2021**, *9*, 1591–1604. [CrossRef]

20.　Zhang, Z.; Liu, Y.; Liang, X.; Guo, H.; Zhuang, X. Robust Model Predictive Current Control of PMSM Based on Nonlinear Extended State Observer. *IEEE J. Emerg. Sel. Top. Power Electron.* **2023**, *11*, 862–873. [CrossRef]

21.　Wang, W.; Liu, C.; Song, Z.; Dong, Z. Harmonic Current Suppression for Dual Three-Phase PMSM Based on Deadbeat Control and Disturbance Observer. *IEEE Trans. Ind. Electron.* **2023**, *70*, 3482–3492. [CrossRef]

22.　Yu, K.; Wang, Z. Improved Deadbeat Predictive Current Control of Dual Three-Phase Variable-Flux PMSM Drives With Composite Disturbance Observer. *IEEE Trans. Power Electron.* **2022**, *37*, 8310–8321. [CrossRef]

23.　Carlet, P.G.; Tinazzi, F.; Bolognani, S.; Zigliotto, M. An Effective Model-Free Predictive Current Control for Synchronous Reluctance Motor Drives. *IEEE Trans. Ind. Appl.* **2019**, *55*, 3781–3790. [CrossRef]

24.　Agoro, S.; Husain, I. Model-Free Predictive Current and Disturbance Rejection Control of Dual Three-Phase PMSM Drives Using Optimal Virtual Vector Modulation. *IEEE J. Emerg. Sel. Top. Power Electron.* **2023**, *11*, 1432–1443. [CrossRef]

25.　Zhang, Y.; Jin, J.; Huang, L. Model-Free Predictive Current Control of PMSM Drives Based on Extended State Observer Using Ultralocal Model. *IEEE Trans. Ind. Electron.* **2021**, *68*, 993–1003. [CrossRef]